

# icemc: A Monte Carlo Simulation for Cosmogenic Neutrinos interacting in the Antarctic ice as viewed by the Antarctic Impulsive Transient Antenna (ANITA)

---

## ANITA Collaboration

L. Cremonesi<sup>ucl</sup> A. Connolly<sup>osu</sup> P. Allison<sup>osu</sup> O. Banerjee<sup>osu</sup> L. Batten<sup>ucl</sup> J. J. Beatty<sup>osu</sup>  
K. Bechtol<sup>uc,lst</sup> K. Belov<sup>jpl</sup> D. Z. Besson<sup>ku,mephi</sup> W. R. Binns<sup>wu</sup> V. Bugaev<sup>wu</sup> P. Cao<sup>ud</sup>  
C. C. Chen<sup>ntu</sup> C. H. Chen<sup>ntu</sup> P. Chen<sup>ntu</sup> J. M. Clem<sup>ud</sup> B. Dailey<sup>osu</sup> C. Deaconu<sup>uc</sup>  
P. F. Dowkontt<sup>wu</sup> B. D. Fox<sup>uh</sup> J. W. H. Gordon<sup>osu</sup> P. W. Gorham<sup>uh</sup> B. Hill<sup>uh</sup> J. J. Huang<sup>ntu</sup>  
K. Hughes<sup>osu,uc</sup> R. Hupe<sup>osu</sup> M. H. Israel<sup>wu</sup> K. M. Liewer<sup>jpl</sup> S. Y. Lin<sup>ntu</sup> T. C. Liu<sup>ntu</sup>  
A. Ludwig<sup>uc</sup> L. Macchiarulo<sup>uh</sup> S. Matsuno<sup>uh</sup> K. McBride<sup>osu</sup> C. Miki<sup>uh</sup> K. Mulrey<sup>ud,brus</sup>  
J. Nam<sup>ntu</sup> R. J. Nichol<sup>ucl</sup> A. Novikov<sup>ku,mephi</sup> E. Oberla<sup>uc</sup> S. Prohira<sup>osu</sup> B. F. Rauch<sup>wu</sup>  
J. M. Roberts<sup>uh,ucsd</sup> A. Romero-Wolf<sup>jpl</sup> B. Rotter<sup>uh</sup> J. W. Russell<sup>uh</sup> D. Saltzberg<sup>ucla</sup>  
D. Seckel<sup>ud</sup> H. Schoorlemmer<sup>uh,mpl</sup> J. Shiao<sup>ntu</sup> S. Stafford<sup>osu</sup> J. Stockham<sup>ku</sup> M. Stockham<sup>ku</sup>  
B. Strutt<sup>ucla</sup> J. Stuhr<sup>calpoly</sup> G. S. Varner<sup>uh</sup> A. G. Viereggs<sup>uc</sup> S. H. Wang<sup>ntu</sup> S. A. Wissel<sup>calpoly</sup>

<sup>uc</sup>Dept. of Physics, Enrico Fermi Inst., Kavli Inst. for Cosmological Physics, Univ. of Chicago, Chicago, IL 60637.

<sup>ucla</sup>Dept. of Physics and Astronomy, Univ. of California, Los Angeles, Los Angeles, CA 90095.

<sup>osu</sup>Dept. of Physics, Center for Cosmology and AstroParticle Physics, Ohio State Univ., Columbus, OH 43210.

<sup>uh</sup>Dept. of Physics and Astronomy, Univ. of Hawaii, Manoa, HI 96822.

<sup>ntu</sup>Dept. of Physics, Grad. Inst. of Astrophys., & Leung Center for Cosmology and Particle Astrophysics, National Taiwan University, Taipei, Taiwan.

<sup>ku</sup>Dept. of Physics and Astronomy, Univ. of Kansas, Lawrence, KS 66045.

<sup>mephi</sup>National Research Nuclear University, Moscow Engineering Physics Institute, 31 Kashirskoye Highway, Russia 115409.

<sup>wu</sup>Dept. of Physics and McDonnell Center for the Space Sciences, Washington Univ. in St. Louis, MO 63130.

<sup>slac</sup>SLAC National Accelerator Laboratory, Menlo Park, CA, 94025.

<sup>ud</sup>Dept. of Physics, Univ. of Delaware, Newark, DE 19716.

<sup>ucl</sup>Dept. of Physics and Astronomy, University College London, London, United Kingdom.

<sup>jpl</sup>Jet Propulsion Laboratory, Pasadena, CA 91109.

<sup>calpoly</sup>Physics Dept., California Polytechnic State Univ., San Luis Obispo, CA 93407.

<sup>mpl</sup>Max-Planck-Institut für Kernphysik, 69117 Heidelberg, Germany.

<sup>brus</sup>Astrophysical Institute, Vrije Universiteit Brussel, Pleinlaan 2, 1050, Brussels, Belgium.

<sup>lst</sup>LSST, 950 North Cherry Avenue, Tucson, AZ 85721

<sup>ucsd</sup>Center for Astrophysics and Space Sciences, Univ. of California, San Diego, La Jolla, CA 92093

**ABSTRACT:** A Monte Carlo simulation tool for the radio detection of Ultra High Energy (UHE) neutrino interactions in the Antarctic ice, *icemc*, is described in this article. This tool includes the simulation of UHE neutrinos, the parametrization of the Askaryan radiation generated by their interaction in the ice, and the propagation of the radiation through ice and air to a simulated model of the third and fourth ANITA (Antarctic Impulsive Transient Antenna) flights. This paper provides an overview of the *icemc* simulation, a detailed description of the physics models used, data/simulation comparisons to validate the physics performance, and a summary of the impact of published results. Finally the sensitivity of the fourth ANITA flight is presented. If no neutrinos are detected, ANITA is expected to improve upon its world leading limit on the cosmogenic neutrino flux above  $10^{19}$  eV.

**KEYWORDS:** neutrino radio detection, ultra-high-energy, Monte Carlo

**ARXIV EPRINT:** ...

---

## Contents

<b>1</b>	<b>Introduction</b>	<b>2</b>
<b>2</b>	<b>The ANITA flights</b>	<b>4</b>
<b>3</b>	<b>Event geometry</b>	<b>6</b>
3.1	Modeling the Antarctic continent	6
3.2	Picking interaction point and direction	6
3.3	Event weighting	6
<b>4</b>	<b>Radio signal simulation</b>	<b>7</b>
4.1	Askaryan parametrization	7
4.2	Neutrino flavors and interaction types	7
4.3	Cherenkov Cone	8
<b>5</b>	<b>Propagation in ice and air</b>	<b>8</b>
<b>6</b>	<b>ANITA detector model</b>	<b>9</b>
6.1	Tunable Universal Filter Front-end boards	10
6.2	Thermal noise	11
6.3	Trigger simulation	12
<b>7</b>	<b>Validation</b>	<b>14</b>
7.1	Comparisons with lab measurements	14
7.1.1	Trigger efficiency scans	14
7.2	Comparisons with flight measurements	16
7.2.1	Thermal noise validation	16
7.2.2	WAIS pulser model	17
7.2.3	Reconstruction validation	18
<b>8</b>	<b>ANITA sensitivity</b>	<b>19</b>
8.1	Acceptance	19
8.2	Limit	21
<b>9</b>	<b>Summary and Future improvements</b>	<b>21</b>
<b>10</b>	<b>Acknowledgements</b>	<b>22</b>
<b>A</b>	<b>Obtaining and using icemc</b>	<b>25</b>

---

# 1 Introduction

The ANtarctic Impulsive Transient Antenna (ANITA) experiment is a NASA-funded, balloon-borne experiment aiming primarily to detect Ultra-High-Energy (UHE) neutrinos and cosmic rays [1–4]. UHE neutrinos may be produced when cosmic rays interact with the cosmic microwave background, either through the Greisen Zatsepin Kuzmin (GZK) [5, 6] mechanism or through photo-disintegration, or directly from an astrophysical source. UHE neutrinos interact in the Antarctic ice and produce a coherent radio pulse of Askaryan radiation [7]. UHE cosmic rays interact with the geomagnetic field to produce a coherent radio impulse [8–10]. The geometry of the Earth’s magnetic field in Antarctica allows ANITA to distinguish the signatures of these two types of events through their polarization.

The ANITA experiment flies approximately 40 km above Antarctica looking for radio signals in the band between 200 and 1200 MHz, produced by UHE neutrinos and cosmic rays. Figure 1 shows a basic scheme of the Askaryan neutrino detection at the ANITA experiment, as well as the UHE cosmic ray detection principle. Four ANITA flights (Section 2) have been successfully completed so far, and this paper focuses on the simulations of the third and fourth ANITA flights.

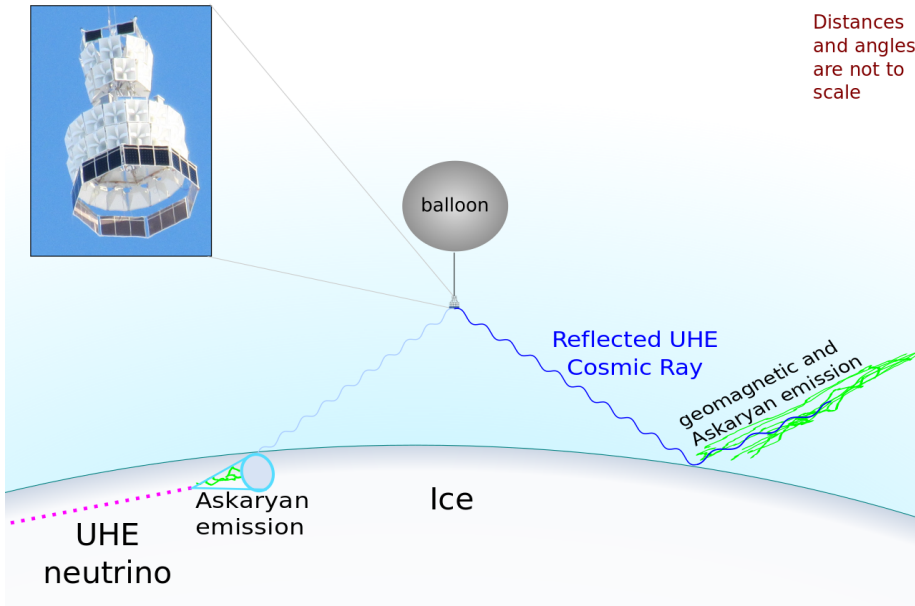


**Figure 1.** The ANITA detection concept with a photo of the ANITA-IV payload. UHE neutrinos interact with the Antarctic ice and produce a coherent radio pulse of Askaryan radiation. UHE cosmic ray interactions in the atmosphere produce a shower of secondary particles that interact with the geomagnetic field to produce a coherent radio impulse. These signals are detected by the ANITA instrument, given its position on a NASA long duration balloon.

The `icemc` program is a C++ Monte Carlo simulation tool based on ROOT [11] used to simulate UHE neutrino interactions producing Askaryan radiation. This tool is used by the ANITA collaboration to tune the neutrino analysis selection and quantify the experiment’s sensitivity.

A flowchart of the `icemc` simulation steps is shown in Figure 2. At the beginning of each run the user can choose which ANITA flight to simulate and which neutrino energy spectrum to use. For

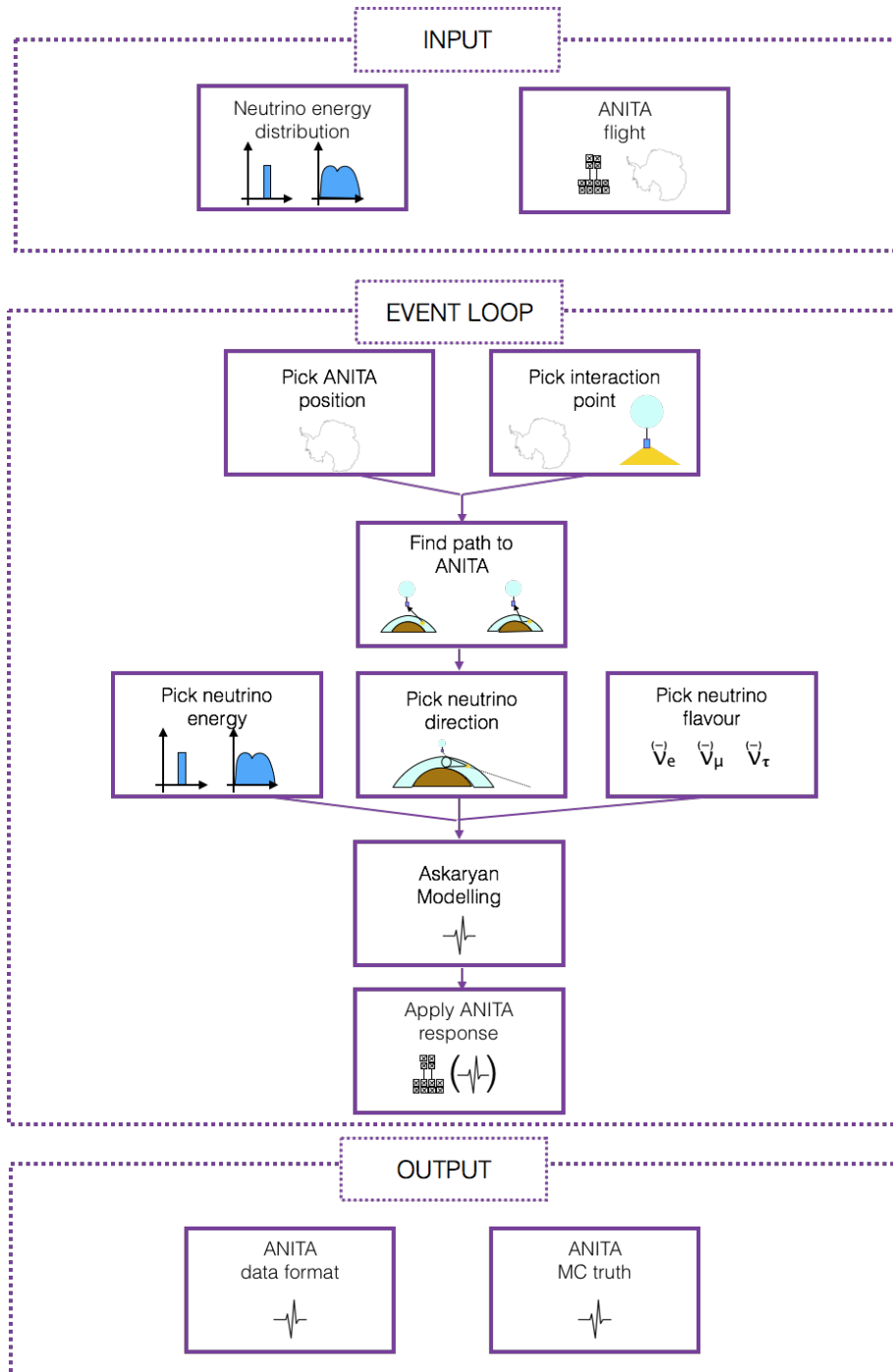


**Figure 2.** Flowchart of the *icemc* simulation for a single candidate.

each neutrino event, the position of the payload along the ANITA flight path, as well as the neutrino interaction position are randomly chosen. These are used to find the path to the ANITA detector (Section 3). The neutrino direction is then chosen within detectable angles; the neutrino energy is chosen following the input theoretical model; and the neutrino flavour and interaction type are

chosen according to their expected ratios. These parameters are used to produce the radio-frequency pulse following the Askaryan model described in Section 4. The signal is then propagated through the ice and air to the ANITA detector (see Section 5). The response of the ANITA signal chain is simulated, and the resulting data are saved in the same format as ANITA flight data (see Section 6). Different parts of the simulation are validated against data taken both in the lab and in-flight during the past ANITA flights (see Section 7). Finally the neutrino acceptance of the third and fourth ANITA flights, and the contributions of the different parts of the simulation to the uncertainties on the acceptance are presented in Section 8.

## 2 The ANITA flights

The first two ANITA payloads flew in 2006-2007[2] and 2008-2009[3, 4], respectively. Although `icemc` can be used to simulate older flights, this paper focuses on the simulation of the third and fourth flights.

Figure 3 shows the flight paths of the ANITA-III and ANITA-IV instruments. The color map shows the Antarctic ice depth. The third ANITA payload (ANITA-III) launched on December 18<sup>th</sup>, 2014 from the NASA Long Duration Balloon (LDB) facility near McMurdo Station, Antarctica. ANITA-III followed the polar vortex flying at the altitude of 37 km for 22 days until January 9<sup>th</sup>, 2015 when the flight was terminated near the Australian Davis Station. Similarly, the fourth ANITA payload (ANITA-IV) launched on December 2<sup>nd</sup>, 2016 from the NASA LDB facility in Antarctica and landed approximately 100 km from the South Pole Station on December 29<sup>th</sup>, 2016.

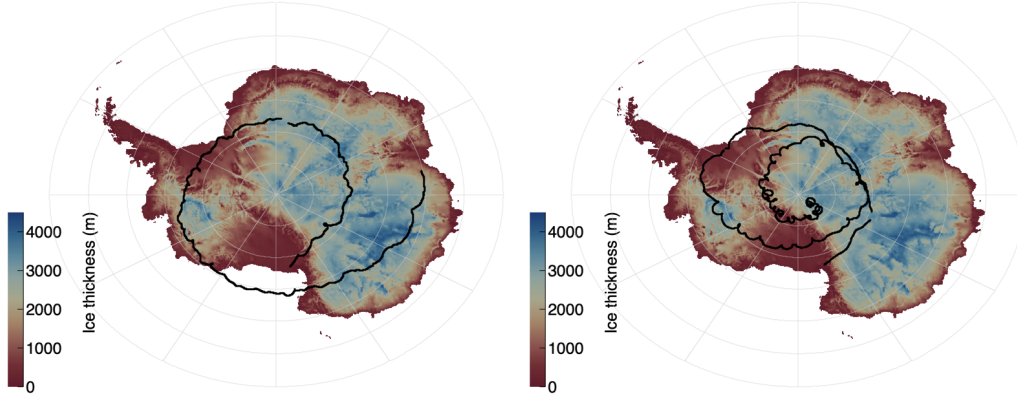


**Figure 3.** Flight path simulated in `icemc` for the ANITA-III (left) and ANITA-IV (right) flights. Antarctica map produced using the BEDMAP model [12].

The ANITA-III and ANITA-IV instruments were similar to the two previous ones [2, 3], using 48 dual-polarization quad-ridged horn antennas with bandwidth from 200 to 1200 MHz. The antennas were arranged in three rings forming 16 azimuthal sectors per ring, with the top ring divided into two layers to fit the launch envelope specifications, as shown in Figure 1.

Figure 4 shows a schematic of the ANITA-III signal chain. The receiving antenna measures vertical and horizontal polarization components of incident radio waves, which then follow twin paths. After passing through filters and amplifiers, the signal is split into the trigger and digitizer

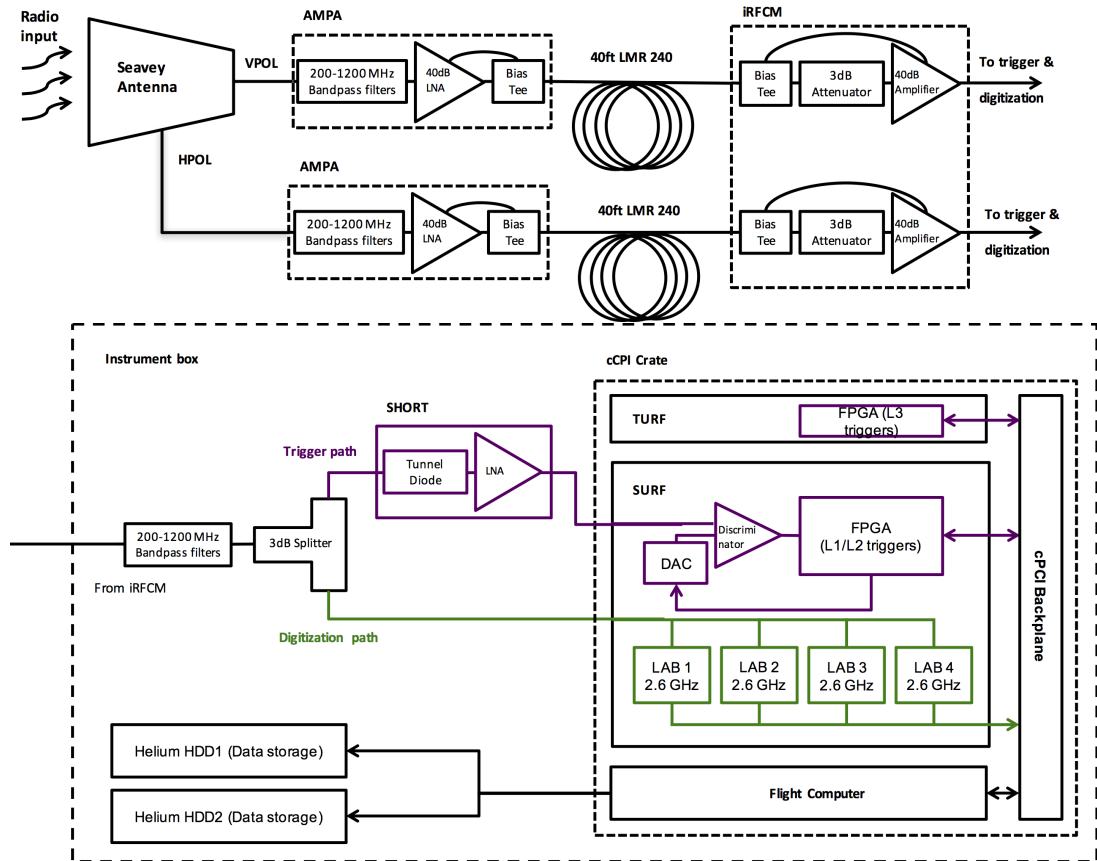


**Figure 4.** ANITA-III signal chain. The receiving antenna splits signals into vertical and horizontal polarizations which follow identical paths. After going through filters and amplifiers, the signal is split into the trigger and digitizer paths. In the trigger path the signal passes through a tunnel diode and is compared to a threshold. When a trigger is issued, a switched capacitor array digitizes the signal with a mean sample rate of 2.6 GSa/s.

paths. In the trigger path the signal passes through a tunnel diode which acts as a square-law detector over the input. The output of the tunnel diode is compared to the channel threshold, which is dynamically adjusted by a PID loop to maintain the rate for each antenna around 500 kHz. A combination of first-level (L1) and second-level (L2) triggers forms a global trigger which can be issued in each polarization. When a trigger is issued, a switched capacitor array digitizes the signal with a mean sample rate of 2.6 GSa/s. The ANITA-IV signal chain included the Tunable Universal Filter Frontend boards (see Subsection 6.1), and 90° hybrids to convert the signals into left- and right- circularly polarized (LCP and RCP) components. The ANITA-IV trigger logic also required a coincidence between LCP and RCP signals within a 4 ns coincidence window to select for linearly polarized signals.

As the payload rotates freely, two sets of GPS units were used to independently determine the payload position and attitude. Power was supplied by an octagonal array of photovoltaic panels and stored using four pairs of 12-V lead-acid batteries. Communication to and from the payload was through the Iridium and TDRSS satellite systems throughout the flight, and by a direct line-of-sight

radio link when within range of McMurdo Station.

### 3 Event geometry

#### 3.1 Modeling the Antarctic continent

Crust 2.0 [13] is used to model the Earth's interior near the surface. It is based on seismological data published from the Cooperative Studies of the Earth's Deep Interior (CSEDI). The model gives thicknesses and densities of seven material layers in  $2^\circ \times 2^\circ$  bins: ice, water, soft sediments, hard sediments, upper crust, middle crust, and lower crust.

The total Antarctic ice volume is computed by summing the product of ice thickness and surface area for each bin within the Antarctic continent. The area of each bin is calculated following:

$$\int_{\phi_1}^{\phi_2} \int_{\theta_1}^{\theta_2} \sin \theta \, d\theta \, d\phi = (\phi_2 - \phi_1) \times (\cos \theta_1 - \cos \theta_2), \quad (3.1)$$

where the limits of the integrals define the edges of the bin in latitude and longitude. It is also possible to run the simulation using BEDMAP ice thickness and subglacial topographic model of Antarctica, developed by the British Antarctic Survey [12]. This model has a much more accurate representation of the ice in Antarctica, but it is much slower to run, so by default we use Crust 2.0. Using Crust 2.0, the `icemc` program finds  $2.976 \times 10^{16} \text{ m}^3$  of Antarctic ice in this model, compared to  $3.011 \times 10^{16} \text{ m}^3$  reported by the US Geological Survey [14], a 1.15% difference.

#### 3.2 Picking interaction point and direction

For each neutrino event, the payload position is chosen at random from a set of positions along the ANITA flight path (see Figure 3). To simulate only those neutrino interactions that might lead to a detectable signal, interaction positions are limited to occur within the horizon as seen by the payload (roughly between 700 and 800 km from the payload), and neutrino directions are chosen from an annulus on the sky consistent with viewing angles detectable at the payload (see Section 3.3). The maximum angle that the ray may diverge from the axis of the Cherenkov cone for the interaction to still be detectable depends on the electric field, the distance from the interaction to the payload, and shower nature: this is typically between 10 and 13 degrees.

Both direct and reflected detection is simulated. In the first case the signal is propagated from the interaction position upwards to the payload. In the second case, the signal is propagated downwards towards to the ice-rock interface, approximated as a flat mirror, where the signal is then reflected upwards towards the payload.

#### 3.3 Event weighting

To minimize computation time, each event is weighted according to the probability of the neutrino reaching the interaction point without being absorbed in the earth, as well as the "phase space" reduction (defined below), such that only those topologies that give measurable signal are fully simulated. As a neutrino moves through the earth, it encounters varying densities as it passes through layers of the earth's interior, and thus differing interaction lengths. The neutrino survival probability is thus calculated from the along-track water-equivalent amount of material traversed.

The phase space factor is the product of the weights derived from the neutrino interaction position and neutrino direction. These weights are assumed to be independent of one another. The position weight arises due to the neutrino interaction position being chosen only within the payload horizon. This is calculated as the ratio of the volume of ice within the horizon for the  $i^{\text{th}}$  event and the total volume of ice in Antarctica (ratio of the yellow to blue volumes in Figure 5). The neutrino direction is chosen such that the axis of the Cherenkov cone lies close in solid angle to the direction from the interaction point to the payload. The direction weight is calculated as the ratio of the solid angle coming from the Cherenkov cone and a unit sphere (see purple cone in Figure 5).

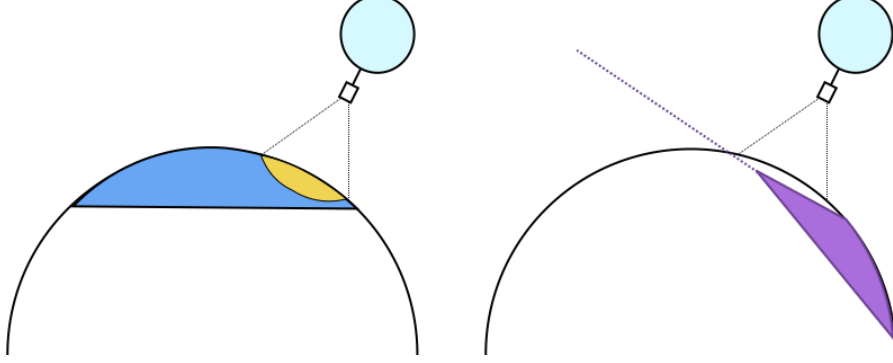


**Figure 5.** A schematic of the phase space weights used in `icemc`. The position weight arises because only interaction positions within the balloon horizon are simulated (yellow over blue area). The direction weight arises because only favourable directions around the Cherenkov cone are simulated (purple angle over a unit sphere).

## 4 Radio signal simulation

### 4.1 Askaryan parametrization

For each event the neutrino energy is picked randomly following the input energy spectrum. Rather than simulating the particle shower development in the ice that would produce the Askaryan radiation, a 1D parametrization is used to get the peak of the Askaryan signal at 1 m from the point of interaction,  $\mathcal{E}^{(@1\text{m})}$ , according to Reference [15] and following:

$$\mathcal{E}^{(@1\text{m})} = 2.53 \times 10^{-7} \cdot \frac{\sin \theta_{\text{view}}}{\sin \theta_{\text{Ch}}} \cdot \frac{E}{\text{TeV}} \cdot \frac{\nu}{\nu_0} \cdot \frac{1}{1 + \left(\frac{\nu}{\nu_0}\right)^{1.44}}, \quad (4.1)$$

where  $\nu$  is the frequency,  $\nu_0 = 1.15$  GHz,  $E$  is the shower energy (see Subsection 4.2),  $\theta_{\text{view}}$  is the viewing angle and  $\theta_{\text{Ch}}$  is the Cherenkov angle. This parametrization is valid up to 5 GHz, covering the ANITA band of 0.2-1.2 GHz.

### 4.2 Neutrino flavors and interaction types

The `icemc` program assumes flavor democracy, assuming the flavors are fully mixed before the neutrinos get to the ice. Information about each flavor is stored separately so the sensitivity to each flavor may be quoted separately.

The neutrino event undergoes a charged/neutral current interaction in 69%/32% of cases. For charged current electron neutrino interactions, the electromagnetic component is calculated as  $1 - y$ , where  $y$  is the inelasticity and is approximated by a double-exponential function [16]. In all other cases the electromagnetic component is considered negligible. The hadronic component is equal to the inelasticity. Secondary particles are not propagated.

### 4.3 Cherenkov Cone

The width of the Cherenkov cone is parametrized separately for the electromagnetic and hadronic components of the shower, according to References [15] and [17], respectively. The width of the electromagnetic component in degrees is characterized by:

$$\Delta\theta_{em}(\nu) = 2.7^\circ \cdot \frac{\nu_0}{\nu} \cdot \left( \frac{E_{LPM}}{0.14E_{EM} + E_{LPM}} \right)^{0.3}, \quad (4.2)$$

where  $E_{EM}$  is the part of the shower energy associated with electromagnetic particles, and  $E_{LPM}$  is energy above which the Landau-Pomeranchuk-Migdal (LPM) effect becomes important. The LPM effect causes the bremsstrahlung interaction to become suppressed because the momentum transfer ( $\propto k/E^2$ ) becomes so small that the Heisenberg uncertainty causes the interaction to occur over many scattering centers, resulting in destructive interference. This effect reduces the width of the Cherenkov cone, but not the magnitude of the electric field at the Cherenkov angle. Following the recommendation in Reference [15],  $E_{LPM}$  is set to  $2 \times 10^{15}$  eV and can be scaled to other media using the ratio of the respective radiation lengths.

The width of the Cherenkov cone for hadronic showers is modeled as laid out in Equation 9 in [17]:

$$\Delta\theta_{had}(\nu) = \frac{c}{\nu} \cdot \frac{\rho}{K_\Delta X_0} \cdot \frac{1}{n^2 - 1}, \quad (4.3)$$

where  $c$  is the speed of light,  $\nu$  is the frequency considered,  $\rho$  is the density of ice,  $K_\Delta$  is a normalization constant determined by a separate Monte Carlo simulation [17],  $X_0$  is the radiation length, and  $n$  is the index of refraction.

The signal strength at viewing angle  $\theta$  away from the Cherenkov angle  $\theta_{Ch}$  is also parametrized following Equation 13 in Reference [17]:

$$\mathcal{E}(\theta) = \frac{\sin \theta}{\sin \theta_{Ch}} \cdot \mathcal{E}(\theta_{Ch}) \cdot \exp \left[ - \left( \frac{\theta - \theta_{Ch}}{\Delta\theta_{em, had}} \right)^2 \right]. \quad (4.4)$$

## 5 Propagation in ice and air

The electric field is propagated to the payload using a standard ray tracing algorithm. The electric field magnitude at the payload position (before applying the ANITA instrument response) is calculated as follows:

$$\mathcal{E}_{\perp, ||} = \mathcal{E}^{(@1m)} e^{(-d_{ice} / \ell_{attn})} \frac{t_{\perp, ||}}{d_{ice} + d_{air}} F(\theta_{view} - \theta_{Ch}). \quad (5.1)$$

The first factor after  $\mathcal{E}^{(@1m)}$  accounts for propagation in ice, with  $d_{ice}$  being the path length and  $\ell_{attn}$  the attenuation length in ice. The second factor accounts for the refraction from ice to air,

using the specular Fresnel coefficients,  $t_{||}$  and  $t_{\perp}$ , for the parallel and perpendicular components of the normalized transmitted electric field vector at the ice-air interface with respect to the local surface normal. The surface normal includes a Gaussian 1.2% direction perturbation to account for surface slope effects. Finally,  $F(\theta_{\text{view}} - \theta_{\text{Ch}})$  is a geometrical attenuation factor of the field strength in air resulting from viewing the Cherenkov emission “off-cone” at an angle  $\theta_{\text{view}}$  different from the Cherenkov angle  $\theta_{\text{Ch}}$ . The functional form of  $F$  is taken to be Gaussian and is set to zero for  $(\theta_{\text{view}} - \theta_{\text{Ch}}) > 20 \Delta\theta_{\text{Ch}}$ , where  $\Delta\theta_{\text{Ch}}$  is the width of the Cherenkov cone.

Cherenkov radiation is radially polarized, and the in-ice polarization vector is calculated using the neutrino velocity vector and in-ice propagation vector, which lies radially outward from the Cherenkov cone. Attenuation lengths for radio in Antarctica are based on measurements performed at the Ross Ice Shelf and the South Pole [18]. The index of refraction is taken as 1.79 for deep ice and 1.325 at the surface. A model for the firn based on data taken by the RICE Collaboration [19] is used at depths shallower than 150 m.

Surface roughness acts to allow different portions of the ice surface to contribute transmitted power to the payload for a single event, due to new allowable scattering geometries at the air-ice interface. The University of Hawaii ANITA group developed a simulation program, used for the ANITA-I and ANITA-II flights, which included surface roughness effects. They found that ice surface roughness contributed to an increase in acceptance of roughly a factor of 50% at low energy (close to  $10^{18}$  eV) and 40% at higher energy. `icemc` currently does not include ice surface roughness effects, and hence conservatively underestimates the sensitivity of the ANITA flights. Future versions of `icemc` will include these effects.

## 6 ANITA detector model

Taking into account the payload rotation, the simulated signal is propagated to the front of each of the ANITA antennas and through the trigger and digitizer paths of the ANITA instrument. The payload position chosen along the flight path is used to load appropriate information about the payload rotation, channel threshold values and channel masking. The payload geometry is simulated using photogrammetry measurements and phase-center calibration measurements taken with a ground pulser during the flights. Antenna gains measured in the lab previous to the flight are applied to the signal according to the incident angles on the E and H planes.

The signal then follows the signal chain as shown in Figure 4. First, the incident fields are folded into the vertical-polarization (VPOL) and horizontal polarization (HPOL) responses of the antennas. The responses of these components are divided into the trigger and digitizer paths. The digitizer and trigger responses were measured using calibration data taken before the flights. Figure 6 (left) shows the power spectra of the trigger and digitizer impulse responses for a sample channel of the ANITA-III payload. To avoid continuous wave (CW) noise from satellite and station transmissions, ANITA-IV adopted tunable notch filters (see Section 6.1 and Reference [20]). Figure 6 (right) shows the power spectra of the trigger and digitizer impulse responses for a sample channel of the ANITA-IV payload with the most common filter configuration used during flight. Thermal noise is generated based on flight measurements (see Section 6.2) and added to the waveforms. The modeled tunnel diode response (see Section 6.3) is convolved with the signal waveforms from all the channels, and if an event passes the trigger logic, the event is saved in the final output.

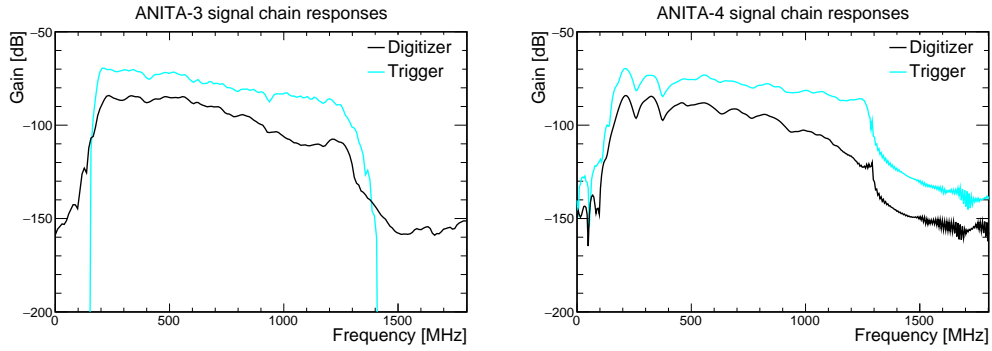


**Figure 6.** Power spectrum of the trigger and digitizer impulse response for a sample channel, for the ANITA-III (left) and ANITA-IV (right) instruments.

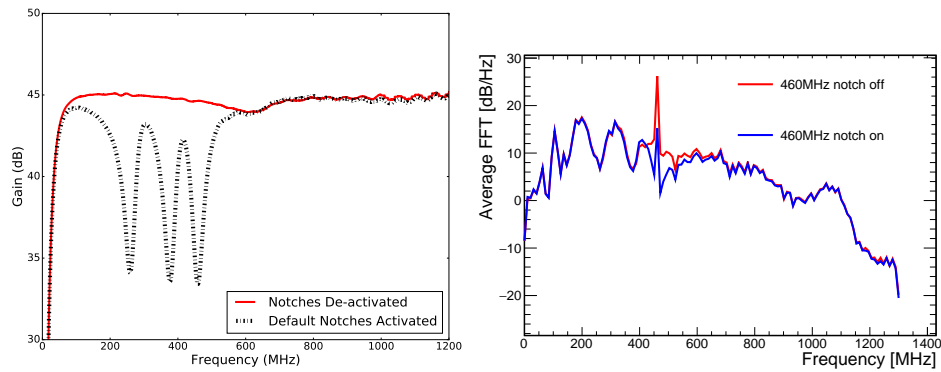


**Figure 7.** (Left) Measured TUFF response in frequency domain (dB vs frequency) obtained in the lab. The dips in the response clearly mark the 260, 375, and 460 MHz notches turned on in this configuration and the 13 dB attenuation at those frequencies is clear [20]. (Right) Example of carrier wave noise injected in `icemc` with the third notch activated and not activated.

## 6.1 Tunable Universal Filter Front-end boards

To alleviate the anthropogenic noise observed in ANITA-III that caused significant amounts of deadtime, ANITA-IV added the Tunable Universal Filter Front-end, or TUFF, boards [20]. This board uses up to three notches to attenuate the gain by a maximum of 13 dB around each notch frequency: the notches are tunable, but default to 260, 375, and 460 MHz, corresponding to known satellite communications frequencies, using LRC circuits. Whether each notch is activated and at which frequency is called a "configuration". There were seven unique configurations for the ANITA-IV flight which are simulated in `icemc`. The response of the trigger for the configuration when all notches are on and at default frequencies is plotted in Figure 7(left). An example of the effect of the third notch switched on or off when 460 MHz carrier wave noise is simulated is shown in Figure 7(right).

The time-dependent response for each channel for a given configuration is loaded into `icemc` and convolved with the trigger and digitizer impulse responses.

## 6.2 Thermal noise

Modeling thermal noise is crucial to the simulation of neutrinos as it affects both the trigger and analysis efficiencies. An accurate model of the thermal noise makes it possible to simulate both the accidental noise triggers and the effect of noise fluctuations on the reconstructed correlation maps used to calculate the event direction in the ANITA analyses [21].

To accurately model the thermal noise during the ANITA flights, events coming from minimum bias triggers during a quiet time of the ANITA-III flight (runs 204-250, approximately 2.5 days) are used to produce power spectra for each digitizer channel using bins of width 10 MHz. As the ANITA-III flight suffered more than the previous flights from continuous wave noise coming from satellites and human bases, frequencies in the ranges 234-286 MHz and 344-410 MHz are filtered out in software analysis using two simple notch filters. Antennas facing the sun were also excluded from the average.

For each channel and each frequency bin a Rayleigh PDF is fit to the data:

$$f(A, \sigma) = \frac{A}{\sigma^2} e^{-A^2/(2\sigma^2)}, \quad (6.1)$$

where  $A$  is the amplitude in the frequency domain (in mV/MHz) and  $\sigma$  is the Rayleigh amplitude in that frequency bin. As most of the carrier wave noise is in the tail of these distributions, the Rayleigh fits are performed only to the rising edge and peak of the distributions. Figure 8(left) shows an example of Rayleigh distribution fits for a sample channel in the frequency bin centred at 710.94 MHz. Events in this sample come from minimum bias triggers during the ANITA-III quiet time.

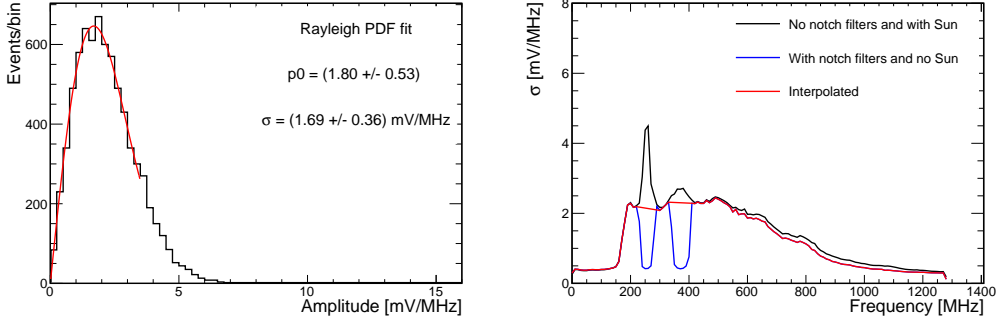


**Figure 8.** Example of a Rayleigh fit for a sample channel in the 710.94 MHz frequency bin (left). The fit is performed only to the rising edge and peak of the distributions, as most CW noise is in the tail. Right: fitted amplitude,  $\sigma(f_i)$ , as a function of frequency (interpolating in the frequency range where power is filtered).

Graphs of the fitted amplitude,  $\sigma(f_i)$ , as a function of frequency were produced for each channel (interpolating in the frequency range where power is filtered), as seen in Figure 8(right). In `icemc` these graphs are used to generate random noise in the frequency domain for each channel: for each frequency bin  $f_i$  the real and imaginary part are randomly extracted from a Gaussian distribution with zero mean and amplitude  $\sigma(f_i)$ , the fitted Rayleigh amplitude in that bin.

This noise is added to the signal in the digitizer path. For the trigger path the noise is re-normalized using the bin-by-bin ratio of the trigger to digitizer path impulse response in the frequency domain before adding it to the signal.

Thermal noise for the ANITA-IV simulation is derived from the ANITA-III measurements, accounting for the different electronics response (including the use of low noise amplifiers and variable filter configurations during the flight) for the two missions. Samples containing only thermal noise are also produced, and they are used in the main ANITA analyses to test the robustness of our analysis selection. Subsection 7.2 details the thermal noise validation for both ANITA flights.

### 6.3 Trigger simulation

The simulation models the L0 trigger by passing the trigger-path signal through a time-domain tunnel diode model and comparing it to the appropriate threshold from the flight for that channel at the event time. The tunnel diode response can be thought of as an integral of the power over about 10 ns, but the true response is non-trivial. The tunnel diode response function is constructed based on the trigger diode output for each channel. The shape of the diode response is described by the sum of two negative Gaussians and a positive function that is the product of a quadratic and an exponential:

$$f(t) = A_1 \cdot e^{-(t-t_0^1)^2/2\sigma_1^2} + A_2 \cdot e^{-(t-t_0^2)^2/2\sigma_2^2} + A_3 \cdot (t-t_0^3)^2 \cdot e^{-(t-t_0^3)/\sigma_3}, \quad (6.2)$$

where the values for the parameters are shown in Table 1;  $f(t)$  is dimensionless. Figure 9 shows the diode response model function.

**Table 1.** Tunnel diode model parameters used for the full band trigger in ANITA-III and ANITA-IV.

	Value 1	Value 2	Value 3
$A$	-0.8	-0.2	0.00964
$\sigma$ [ns]	2.3	4.0	7.0
$t_0$ [ns]	15.0	15.0	18.0

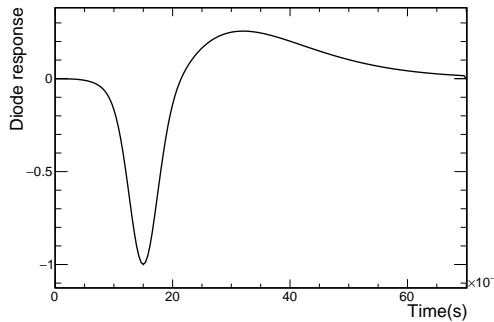


**Figure 9.** Tunnel diode response model used in `icemc`.

For each waveform, the power as a function of time is calculated as:

$$P(t) = \frac{V(t) \cdot V(t)}{Z}, \quad (6.3)$$

where  $V(t)$  is the voltage at time  $t$ , and  $Z = 50 \Omega$  is the system impedance. The next step is to convolve the waveform power with the diode response to find the diode output  $D(t)$ :

$$D(t) = (f * P)(t) . \quad (6.4)$$

For each time bin, the diode output is compared to the channel threshold,  $V_T$ , multiplied by RMS voltage of the diode outputs coming from pure thermal noise,  $V_{RMS}$ , following:

$$D(t) < V_T \cdot V_{RMS} . \quad (6.5)$$

If the power output is more negative than the threshold multiplied by  $V_{RMS}$  at any point, then that channel passes the L0 trigger. See Figure 10 for an example of diode output that does not pass the L0 trigger (left) and that does pass the L0 trigger (right).

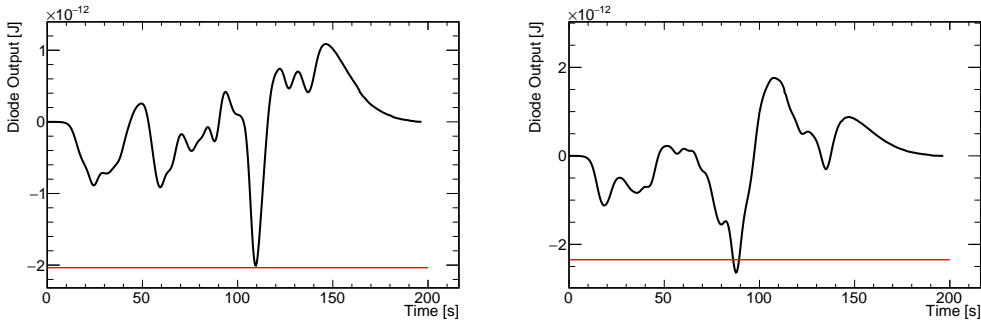


**Figure 10.** Example of diode output that does not pass the L0 trigger (left) and that does pass the L0 trigger (right). The red line shows the value of  $V_T \cdot V_{RMS}$ , showing that the waveform on the right passes the L0 trigger and the waveform on the left does not.

At the beginning of a run,  $V_{RMS}$  is calculated for each channel by simulating 1000 noise waveforms (Subsection 6.2) and sampling the diode output at the center of each waveform (see Figure 11). In ANITA-III, two channels had very large  $V_{RMS}$  associated with them that prevents them from triggering in the simulation: one was broken during the flight, and the other one had an additional filter applied during flight to allow an in-flight calibration pulser to be used.

The trigger logic for the ANITA-III and ANITA-IV triggers is very similar. The main difference is that ANITA-IV used 90 degree hybrids to transform HPOL and VPOL signals into LCP and RCP components of waveforms, so the ANITA-IV L1 trigger requires a LCP and RCP L0 coincidence in the same antenna within one 4 ns clock cycle. The ANITA-III instrument did not have an L1 trigger. The L2 trigger is formed by a coincidence of two out of three antennas (top, middle, bottom) in the same azimuthal sector. As ANITA is intended to look for plane-waves from below, a simple causal requirement is enforced on the coincidence windows. An L1 on the bottom antenna opens a coincidence window open for four FPGA clock cycles (nominally 16 ns). Middle and top L1's open the window for three and one-clock cycles (nominally 12 and 4 ns), respectively (see Figure 12 (left)). Finally, the global trigger is formed by the coincidence of L2 triggers in two adjacent azimuthal sectors (see Figure 12 (right)) within 3 clock cycles. For ANITA-III either polarization or both may produce a global trigger. Either the L2 or global-trigger may be masked for an azimuthal sector if the L2 or global rate is too high in the sector. The actual time-dependent masking status from the flight is used in the simulation.

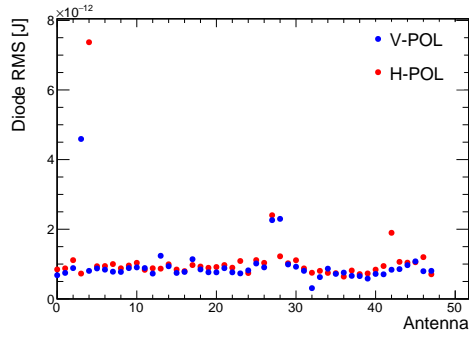


**Figure 11.** Tunnel diode  $V_{RMS}$  for each channel. The two channels with much higher  $V_{RMS}$  are the broken channel, and the channel which had an additional filter applied to accommodate the use of an in-flight calibration system.

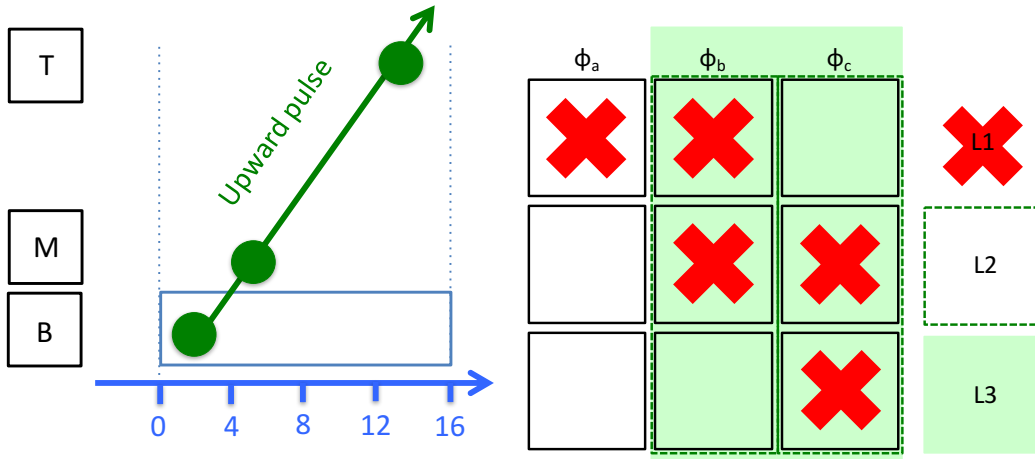


**Figure 12.** Schematic of a second-level trigger example (left), where a plane-wave triggers an antenna in the bottom ring first, and a 16 ns window is opened to check L1 triggers in the middle and top ring. The diagram on the right shows the issuance of a global trigger when two adjacent azimuthal sectors had an L2 trigger.

## 7 Validation

Different parts of the simulation are validated from measurements taken in the lab (Subsection 7.1) and during the flights (Subsection 7.2).

### 7.1 Comparisons with lab measurements

Before each of the ANITA flights, a series of calibration measurements was taken at the NASA Long Duration Balloon Facility near McMurdo Station, Antarctica. These measurements are used to cross-check different parts of the simulation.

#### 7.1.1 Trigger efficiency scans

Trigger efficiency scans are used to measure the ANITA trigger efficiency for signals with different signal-to-noise ratios (SNRs). The setup used before the ANITA-III flights is shown in Figure 13. A

Picosecond Pulse generator is used to produce an RF signal. This is recorded with an oscilloscope and fed directly into the amplifiers behind the ANITA antennas, after going through attenuators and a 12-way splitter. Six of these channels are sent through the trigger and digitizer paths of two azimuthal sectors and are used to measure the global trigger efficiency. One is fed back into the oscilloscope to measure the SNR values.

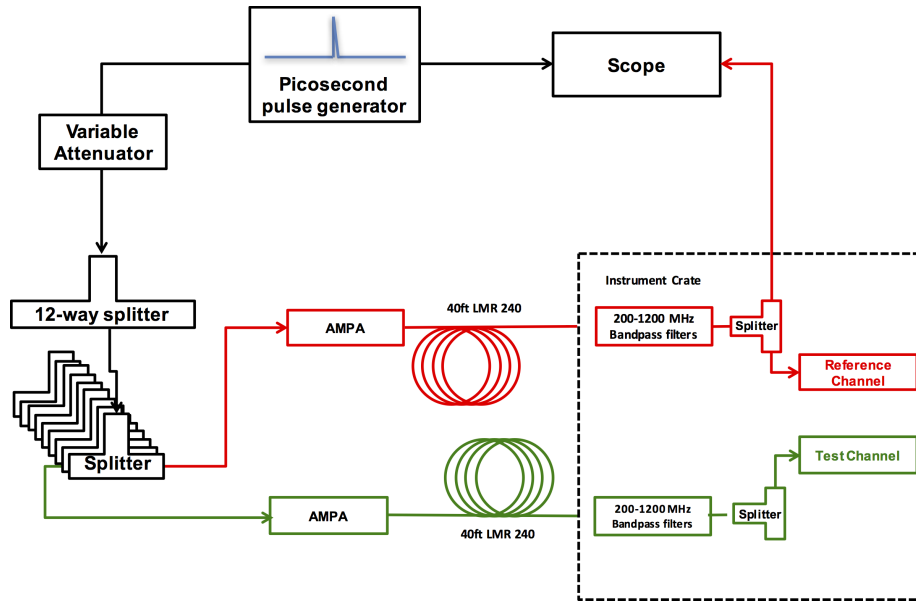


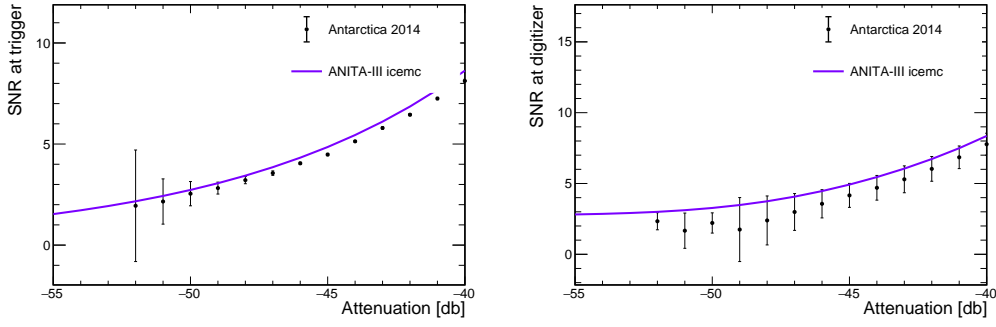
**Figure 13.** Trigger efficiency scans setup in Antarctica before the ANITA-III flight. The signals from the trigger are sent to the oscilloscope via the red line and recorded.

To simulate the trigger efficiency scan setup, the signals measured at the oscilloscope (see Figure 13) are injected into the same six channels used in the data scans, after appropriate attenuation is applied. These go through the trigger/digitizer path and produce ANITA data-like outputs. When simulating trigger efficiency scans, constant power thresholds corresponding to 450 kHz scalers are used for all channels.

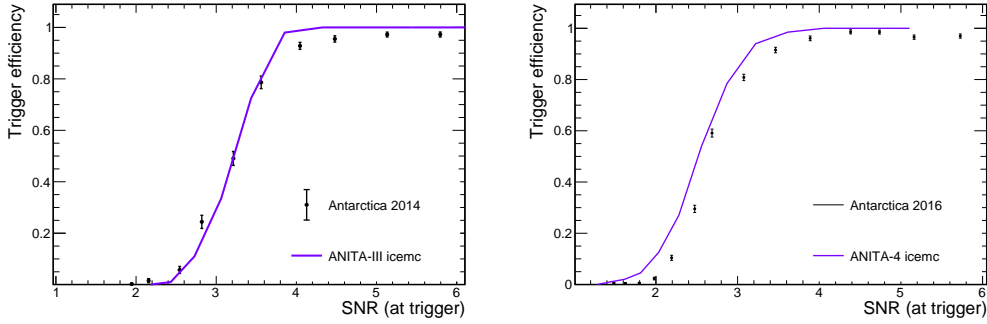
The signals are recorded at the trigger and the digitizer paths are used to validate the simulation. Figure 14 shows a comparison of the measured SNR in data and simulation at the trigger (left) and at the digitizer (right) as a function of the variable attenuation used during the scan. The measured SNR in the digitizer path generally has higher errors compared to the SNR in the trigger path, because the ANITA digitizer has on average a 2.6 GHz sampling rate, whereas the trigger path is measured with a fast oscilloscope.

Figure 15 (left) shows a comparison between data and simulation of a trigger efficiency scan for the ANITA-III payload. The trigger efficiency is plotted as a function of the SNR measured in the trigger path.

Before the ANITA-IV flight, a similar set of measurements was collected at a 6 MHz rate. A data and simulation comparison of the trigger efficiency for the ANITA-IV instrument is shown in Figure 15 (right).



**Figure 14.** SNR measured at the trigger (left) and digitizer (right) as a function of the variable attenuation applied during the trigger efficiency scans. The data points were measured in 2014 in Antarctica prior to the ANITA-III flight.



**Figure 15.** Comparison between data and simulation of a trigger efficiency scan for the ANITA-III (left) and ANITA-IV (right) instruments. The trigger efficiency is plotted a function of the SNR measured at the oscilloscope for the data, and the SNR estimated in the trigger path for the simulation.

## 7.2 Comparisons with flight measurements

Data taken during the ANITA-III and ANITA-IV flights is used to validate the thermal noise, the trigger efficiency to a ground pulser, and the pointing reconstruction.

### 7.2.1 Thermal noise validation

The digitized thermal noise is validated using distributions of the RMS of the simulated waveforms compared to a relatively quiet time during the flights. The ANITA-III quiet time is defined in Subsection 6.2; for the ANITA-IV quiet time, we used forced triggers from run 200. Figure 16 shows the voltage RMS of noise-only waveforms produced in `icemc` compared with the ones coming from a quiet time during the ANITA-III (left) and ANITA-IV (right) flights.

As the ANITA-III data contained a significant amount of carrier wave contamination, a fair comparison of the data and simulation thermal noise is done after applying two notch filters to both datasets, improving the data and simulation agreement. The remaining differences are due to continuous wave noise in the data that could not be simply removed with two notch filters.

The ANITA-IV payload was less affected by carrier wave noise, as the TUFF boards were directly filtering out noisy frequencies, and the requirement of the coincidence between LCP and

RCP signals to form a trigger ensured that only linearly polarized signals triggered the payload. A direct comparison between the measured and simulated noise is seen in Figure 16 (right).

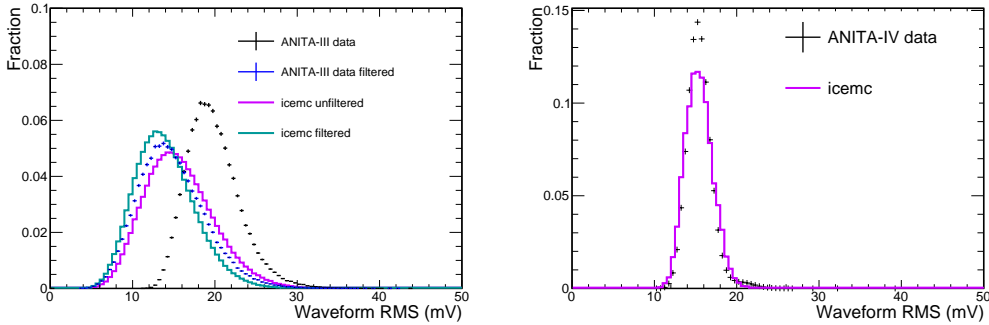


**Figure 16.** Thermal noise validation. Comparison of RMS of waveforms for an icemc simulation and a relatively quiet period of the ANITA-III (left) and ANITA-IV (right) flights. The ANITA-III flight was affected by strong CW noise that for a better comparison has been filtered out. These distributions are normalized to equal area to better compare their shape.

As a second self-consistency check, the ANITA-III simulated thermal noise is also used to produce Rayleigh fits (as described in Subsection 6.2) and shows complete overlap with the fits to the ANITA-III quiet time.

## 7.2.2 WAIS pulser model

As an additional validation, we model the calibration pulser that was located at the West Antarctic Ice Sheet (WAIS) field camp during the ANITA-III and ANITA-IV flights. The WAIS pulser consisted of a 6-kV FID brand pulser that generates a broadband impulse and drives a horizontally polarized antenna. The pulser was triggered on the GPS second with a known delay, permitting a measurement of the ANITA trigger efficiency while the payload is in view of the pulser.

The antenna used at WAIS is a custom design based on a quad-slot model, for which the slots of the antenna are parallel to the ground. The antenna was installed  $\sim 1$  m below the surface of the snow. Similar to a discone, the bottom portion of the antenna acts as a reflector, and the angles of the taper on both the reflector and the upper cone tunes the orientation of the peak gain. This design is a scaled down version of the VHF antenna used as a low frequency extension to ANITA-III.

The WAIS antenna response was modelled using NEC antenna modeling software [22]. Figure 17 shows the peak gain for each frequency, the associated phase at that frequency, and the reflection coefficient,  $\Gamma(f)$ , from this antenna model. We then model the electric field (Figure 17d) generated by the WAIS pulser by convolving the NEC model of the antenna with measurements of the voltage generated by the FID pulser on an oscilloscope. The electric field at 1 m from the pulser,  $E(f)$ , results from relating the power density radiated by the antenna to the power density generated by the pulser with a characteristic impedance  $Z_c$  and voltage  $V(f)$  at the pulser, accounting for loss from imperfect antenna matching between the antenna and the pulser, the magnitude and phase of the gain,  $G(f)$ , propagation loss, and the impedance of free space,  $Z_0$ :

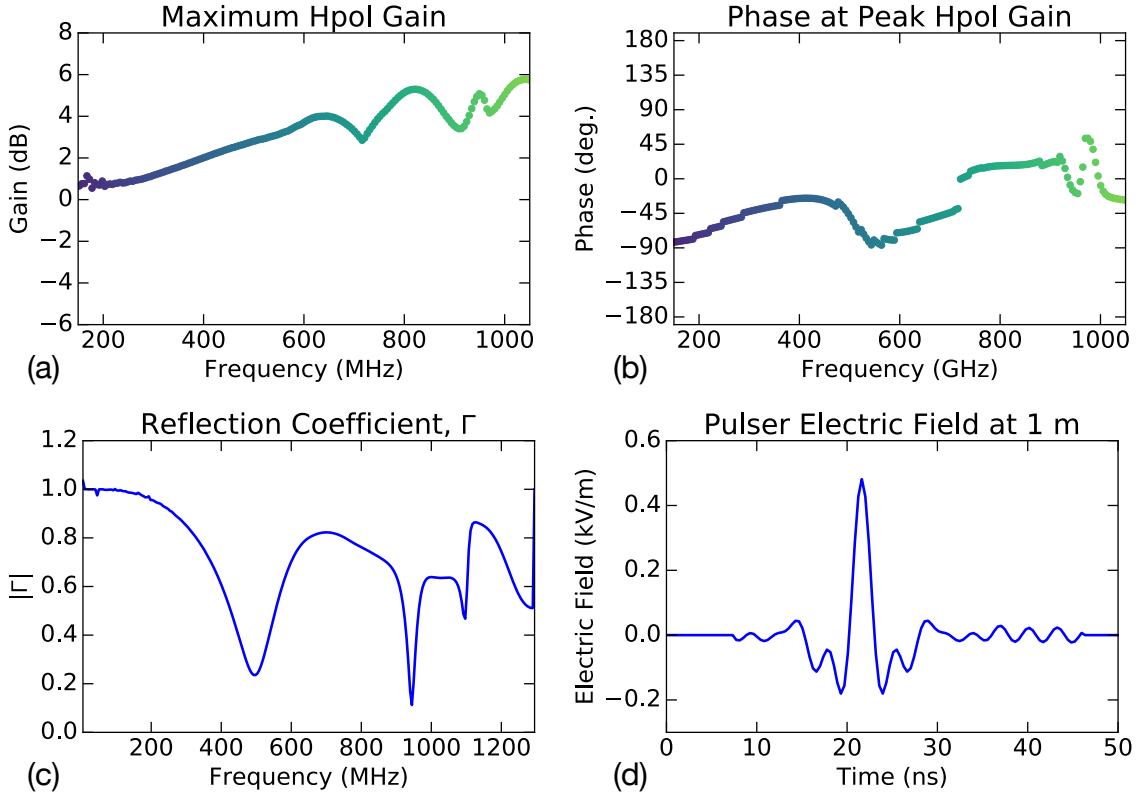


**Figure 17.** Characterization of the ANITA-III horizontally polarized antenna used in the WAIS pulser.

$$|E(f)| = \sqrt{\frac{|V(f)|^2}{8Z_c}(1 - |\Gamma(f)|^2)\frac{Z_0}{2\pi(1\text{ m})^2}G} \quad (7.1)$$

The simulation treats the electric field shown in Figure 17 as originating from a source at the location of the WAIS pulser. Figure 18 shows the efficiency of the ANITA-III payload to generate a trigger from pulses coming from WAIS divide. The simulation efficiency does not asymptote to 1 at high SNR, as it also includes inefficiencies due to the channel masking and the instrument dead time.

### 7.2.3 Reconstruction validation

To fully validate the simulation, a large sample of simulated neutrinos is produced following the cosmogenic neutrino flux arising from a mixed cosmic-ray composition as modeled by Kotera et al. [23]. Simulated waveforms from different triggering channels are cross-correlated to form a pointing map in the ANITA payload coordinates, azimuth ( $\phi_{\text{meas}}$ ) and elevation ( $\theta_{\text{meas}}$ ). The peak of the correlation map is then compared to the expected azimuth ( $\phi_{\text{theory}}$ ) and elevation ( $\theta_{\text{theory}}$ ), calculated from the true neutrino interaction point. Details of our reconstruction and analysis can be found in our previous publications [2, 3, 21].

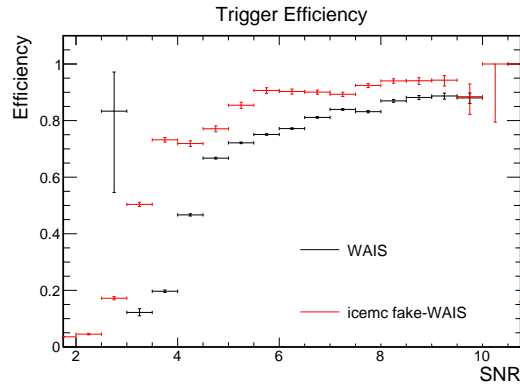


**Figure 18.** ANITA-III trigger efficiency to a pulsar coming from the WAIS divide station as a function of SNR.

## 8 ANITA sensitivity

The simulation files produced with `icemc` are used by the ANITA analysts to tune analysis cuts, check the rate of accidental clustering, and also to simulate sources like Gamma Ray Bursts and Active Galactic Nuclei. Finally, the simulation is used to calculate the experimental sensitivity.

### 8.1 Acceptance

The ANITA collaboration uses `icemc` to calculate the experiment volumetric acceptance  $\langle V\Omega \rangle(E)$ , following:

$$\langle V\Omega \rangle(E) = \frac{n_{pass}(E)V_0\Omega}{N(E)}, \quad (8.1)$$

where  $n_{pass}(E)$  is the weighted (see Section 3.3) number of events that pass the trigger at a given energy  $E$ ,  $V_0$  is the volume of ice in Antarctica viewed by ANITA,  $\Omega$  is  $4\pi$  steradians, and  $N(E)$  is number of neutrinos thrown by each simulation at that energy  $E$ .

The ANITA acceptance ( $\langle A\Omega \rangle(E)$ ) is calculated following:

$$\langle A\Omega \rangle(E) = \frac{\langle V\Omega \rangle(E)}{\ell_{int}(E)}, \quad (8.2)$$

where  $\langle V\Omega \rangle(E)$  is the volumetric acceptance and  $\ell_{int}(E)$  is the average interaction length in that energy bin. The interaction length is calculated following:

$$\ell_{int}(E_\nu) = \frac{M_{NUCL}}{\sigma(E)\rho_{h_2o}}, \quad (8.3)$$

where  $M_{NUCL}$  is the atomic nuclear mass ( $1.66 \cdot 10^{-27}$  kg),  $\rho_{h_2o}$  is the density of water ( $1000$  kg/m<sup>3</sup>), and  $\sigma(E)$  is the neutrino cross-section for  $\nu$  charged-current interactions. Currently the neutrino cross-section is calculated using either the Reno *et al.* [24] or the Connolly *et al.* [25] parametrizations. The latter is the default.

Although recent neutrino cross-section measurements by the IceCube Collaboration reached the multi-TeV scale [26, 27], there are still no measurements at energies above 10 TeV. The current

theoretical models can extrapolate the cross-sections up to  $10^{21}$  eV [24, 25], but the associated uncertainties are large, and the impact on the ANITA acceptance is non-negligible. Figure 19 (right) shows the effect of changing the cross-section parametrization on the ANITA-III acceptance. The nominal Connolly *et al.* parametrization is compared to the upper and lower bound set by Reference [25], and to the alternate parametrization suggested by Reference [24].

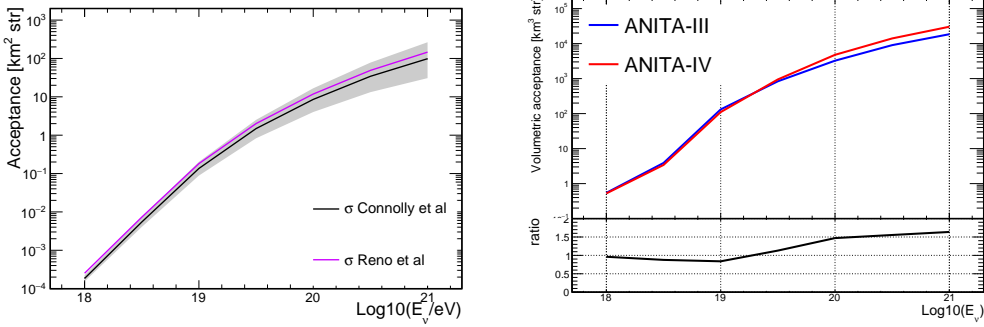


**Figure 19.** (Left) ANITA-III acceptance for different cross-section parametrizations: Connolly et al. [25] and Reno et al. [24]. (Right) ANITA-III and ANITA-IV volumetric acceptance comparison as a function of energy.

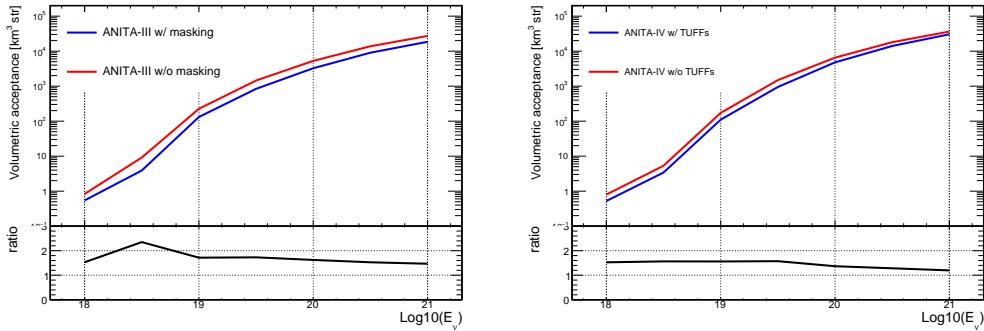


**Figure 20.** (Left) Comparison of ANITA-III volumetric acceptance with and without channel masking. (Right) Comparison of ANITA-IV volumetric acceptance with and without TUFFs.

Figure 19(right) shows the ANITA-III and ANITA-IV volumetric acceptances and their ratio. The ANITA-IV hardware improvements (use of better low noise amplifiers, the tunable notch filters to avoid carrier wave noise, and the use of LCP-RCP trigger coincidences to avoid satellite noise) enabled ANITA-IV to improve by 50% at high energy.

Volumetric acceptances are also used to compare the impact of different hardware choices. ANITA-III was highly affected by satellite noise and had to employ channel masking throughout the entire flight to avoid overloading the trigger. Figure 20 (left) shows that channel masking reduced the ANITA-III sensitivity by more than 50% across all energy bins. ANITA-IV used the TUFF boards to avoid carrier wave noise: Figure 20 (right) shows the impact of the tunable filters on the ANITA-IV sensitivity which was reduced by 25–50%.

Figure 21 shows the variation of the ANITA-IV volumetric acceptances coming from different `icemc` parameter variations. The black solid line shows the effect of using BEDMAP instead of CRUST 2.0 as Antarctica ice model; the more finely binned BEDMAP map results in a roughly 20% lower acceptance over all energies. The orange solid lines shows the effect of varying the random surface inclination, the two cases shows are 0 and 2.4%, where the latter is double the nominal value. The violet area shows the effect of using constant trigger thresholds instead of time varying thresholds; the dashed violet area is the result of using the minimum and maximum thresholds for the whole flight.

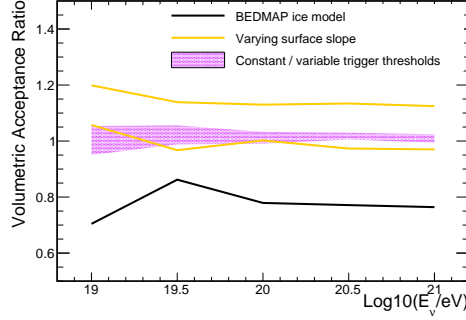


**Figure 21.** Ratio of ANITA-IV volumetric acceptances as a function of energy found varying different `icemc` parameters. The solid black line shows the variation coming from using BEDMAP instead of CRUST 2.0 as Antarctica ice model. The orange solid lines are calculated by setting the surface slope inclination at 0 or 2.4% (double the nominal). The violet dotted area is found by using constant trigger thresholds instead of time varying thresholds.

## 8.2 Limit

The projected 90% confidence level on the diffuse neutrino flux is set by using:

$$\left( \frac{E d^4 N}{dE dA d\Omega dt} \right)_{lim} = \frac{s_{up}}{T \cdot \epsilon_{ana}(E_\nu) \cdot \langle A\Omega \rangle(E) \cdot \Delta}, \quad (8.4)$$

where  $s_{up}$  is the upper (one-sided) limit for the mean of a Poisson variable given 0 observed events in the absence of background for 90% CL,  $T$  is the live time (17.4 days for ANITA-III and 24.25 days for ANITA-IV),  $\epsilon_{ana}(E_\nu)$  is the neutrino analysis efficiency,  $\langle A\Omega \rangle(E)$  is the experiment acceptance as a function of the neutrino energy, and  $\Delta = 4$  is a model-independent factor following Reference [19].

Figure 22 shows the ANITA-III, ANITA-IV and ANITA I-IV limits as calculated in References [28, 29]. These are compared to the latest constraints coming from the IceCube [30] and Auger experiments [31], as well as four cosmogenic neutrino models [32–35].

## 9 Summary and Future improvements

The `icemc` Monte Carlo simulation tool is used for the simulation of ultra high energy neutrino interactions in the Antarctic ice and their detection by the ANITA experiment. The data taken

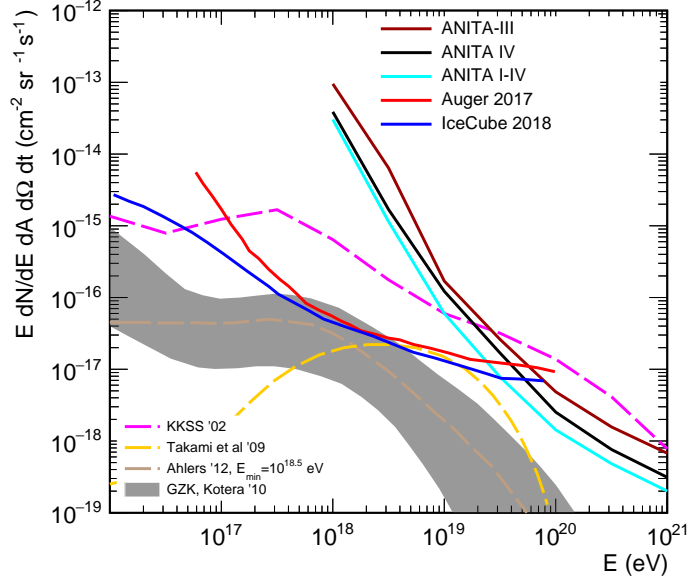


**Figure 22.** ANITA-III and ANITA-IV limit on the all flavor diffuse UHE neutrino flux and a combined limit from ANITA I-IV, as calculated in References [28, 29]. The most recent UHE neutrino limits from the Auger [31] and IceCube [30] experiments, and four cosmogenic neutrino models [32–35] are also displayed.

before or during the ANITA flights are used to validate the simulation. The latest ANITA-III, ANITA-IV and ANITA I-IV performance is provided in the form of the acceptance and energy dependent neutrino limit.

Future versions of the tool will include the possibility to use extensive air showers inputs from ZHAireS [36]; improved and refined ice properties modeling and surface roughness effects; the contribution of the sun to the thermal noise; and carrier wave noise as measured during the ANITA-III and ANITA-IV flights. We are also working towards expanding the framework so that it can be used by all radio experiments based in Antarctica.

## 10 Acknowledgements

We would like to thank the National Aeronautics and Space Administration and the National Science Foundation, especially the Office of Polar Programs. We would especially like to thank the staff of the Columbia Scientific Balloon Facility and the logistical support staff enabling us to perform our work in Antarctica. We are deeply indebted to those who dedicate their careers to help make our science possible in such remote environments. This work was supported by the Kavli Institute for Cosmological Physics at the University of Chicago. Computing resources were provided by the University of Chicago Research Computing Center and the Ohio Supercomputing Center at The Ohio State University. A. Connolly and S. Wissel would like to thank the National Science Foundation for their support through CAREER awards 1255557 and 1752922, respectively. A. Connolly would also like to thank the National Science Foundation for their support through the single-PI grant GRT00049285. O. Banerjee and L. Cremonesi’s work was also supported by

collaborative visits funded by the Cosmology and Astroparticle Student and Postdoc Exchange Network (CASPEN). The University College London group was also supported by the Leverhulme Trust. The Taiwan team is supported by Taiwan's Ministry of Science and Technology (MOST) under its Vanguard Program 106-2119-M-002-011.

## References

- [1] P. W. Gorham, P. Allison, S. W. Barwick, J. J. Beatty, D. Z. Besson, W. R. Binns et al., *The antarctic impulsive transient antenna ultra-high energy neutrino detector: Design, performance, and sensitivity for the 2006-2007 balloon flight*, *Astroparticle Physics* **32** (2009) 10 – 41.
- [2] ANITA collaboration, P. W. Gorham, P. Allison, S. W. Barwick, J. J. Beatty, D. Z. Besson, W. R. Binns et al., *New limits on the ultrahigh energy cosmic neutrino flux from the anita experiment*, *Phys. Rev. Lett.* **103** (Jul, 2009) 051103.
- [3] P. W. Gorham, P. Allison, B. M. Baughman, J. J. Beatty, K. Belov, D. Z. Besson et al., *Observational constraints on the ultrahigh energy cosmic neutrino flux from the second flight of the anita experiment*, *Phys. Rev. D* **82** (Jul, 2010) 022004.
- [4] P. W. Gorham, P. Allison, B. M. Baughman, J. J. Beatty, K. Belov, D. Z. Besson et al., *Erratum: Observational constraints on the ultrahigh energy cosmic neutrino flux from the second flight of the anita experiment [phys. rev. d 82 022004 (2010)]*, *Phys. Rev. D* **85** (Feb, 2012) 049901.
- [5] K. Greisen, *End to the cosmic-ray spectrum?*, *Physical Review Letters* **16** (1966) 748.
- [6] G. Zatsepin, *Gt zatsepin and va kuzmin, jetp lett. 4, 78 (1966).*, *JETP Lett.* **4** (1966) 78.
- [7] G. A. Askar'yan, *Excess negative charge of an electron-photon shower and its coherent radio emission*, *Sov. Phys. JETP* **14** (1962) 441–443.
- [8] D. A. Suprun, P. W. Gorham and J. L. Rosner, *Synchrotron radiation at radio frequencies from cosmic ray air showers*, *Astroparticle Physics* **20** (2003) 157–168.
- [9] H. Falcke and P. Gorham, *Detecting radio emission from cosmic ray air showers and neutrinos with a digital radio telescope*, *Astroparticle Physics* **19** (2003) 477–494.
- [10] S. Hoover, J. Nam, P. Gorham, E. Grashorn, P. Allison, S. Barwick et al., *Observation of ultrahigh-energy cosmic rays with the anita balloon-borne radio interferometer*, *Physical Review Letters* **105** (2010) 151101.
- [11] R. Brun and F. Rademakers, *Root-an object oriented data analysis framework*, *Nuclear Instruments and Methods in Physics Research Section A: Accelerators, Spectrometers, Detectors and Associated Equipment* **389** (1997) 81–86.
- [12] M. B. Lythe and D. G. Vaughan, *Bedmap: A new ice thickness and subglacial topographic model of antarctica*, *Journal of Geophysical Research: Solid Earth* **106** (2001) 11335–11351.
- [13] C. Bassin, G. Laske and G. Masters, *The current limits of resolution for surface wave tomography in north america*, *Eos* **81** (2000) .
- [14] J. G. Ferrigno, R. S. Williams and A. Fox, *Coastal-change and glaciological maps of the antarctic peninsula: U.s. geological survey fact sheet 017-02*, 2005.
- [15] J. Alvarez-Muñiz, R. A. Vázquez and E. Zas, *Calculation methods for radio pulses from high energy showers*, *Phys. Rev. D* **62** (Aug, 2000) 063001.

- [16] R. Gandhi, C. Quigg, M. H. Reno and I. Sarcevic, *Ultrahigh-energy neutrino interactions*, *Astroparticle Physics* **5** (1996) 81–110.
- [17] J. Alvarez-Muñiz, E. Marqués, R. A. Vázquez and E. Zas, *Coherent radio pulses from showers in different media: A unified parametrization*, *Phys. Rev. D* **74** (Jul, 2006) 023007.
- [18] P. Gorham, “Anita smex proposal.”
- [19] I. Kravchenko, C. Cooley, S. Hussain, D. Seckel, P. Wahrlich, J. Adams et al., *Rice limits on the diffuse ultrahigh energy neutrino flux*, *Phys. Rev. D* **73** (Apr, 2006) 082002.
- [20] P. Allison et al., *Dynamic tunable notch filters for the Antarctic Impulsive Transient Antenna (ANITA)*, [1709.04536](#).
- [21] A. Romero-Wolf, S. Hoover, A. Viereg, P. Gorham, P. Allison, S. Barwick et al., *An interferometric analysis method for radio impulses from ultra-high energy particle showers*, *Astroparticle Physics* **60** (2015) 72–85.
- [22] G. J. Burke and A. Poggio, *Numerical electromagnetics code (nec)-method of moments. a user-oriented computer code for analysis of the electromagnetic response of antennas and other metal structures. part 1: Program description-theory. part 2: Program description-code. volume 1. revised*, tech. rep., LAWRENCE LIVERMORE NATIONAL LAB CA, 1981.
- [23] K. Kotera and A. V. Olinto, *The astrophysics of ultrahigh-energy cosmic rays*, *Annual Review of Astronomy and Astrophysics* **49** (2011) 119–153.
- [24] M. H. Reno, *High energy neutrino cross sections*, *Nuclear Physics B-Proceedings Supplements* **143** (2005) 407–413.
- [25] A. Connolly, R. S. Thorne and D. Waters, *Calculation of high energy neutrino-nucleon cross sections and uncertainties using the martin-stirling-thorne-watt parton distribution functions and implications for future experiments*, *Phys. Rev. D* **83** (Jun, 2011) 113009.
- [26] M. Aartsen, G. Hill, A. Kyriacou, S. Robertson, A. Wallace, B. Whelan et al., *Measurement of the multi-teV neutrino interaction cross-section with icecube using earth absorption*, *Nature* **551** (2017) 596.
- [27] M. Bustamante and A. Connolly, *Extracting the energy-dependent neutrino-nucleon cross section above 10 teV using icecube showers*, *Physical Review Letters* **122** (2019) 041101.
- [28] P. Gorham, P. Allison, O. Banerjee, L. Batten, J. Beatty, K. Bechtol et al., *Constraints on the diffuse high-energy neutrino flux from the third flight of anita*, *Physical Review D* **98** (2018) 022001.
- [29] P. Gorham, P. Allison, O. Banerjee, L. Batten, J. Beatty, K. Belov et al., *Constraints on the ultra-high energy cosmic neutrino flux from the fourth flight of anita*, *arXiv preprint arXiv:1902.04005* (2019) .
- [30] M. Aartsen, M. Ackermann, J. Adams, J. Aguilar, M. Ahlers, M. Ahrens et al., *Differential limit on the extremely-high-energy cosmic neutrino flux in the presence of astrophysical background from nine years of icecube data*, *Physical Review D* **98** (2018) 062003.
- [31] E. Zas, *Searches for neutrino fluxes in the eev regime with the pierre auger observatory*, *PoS* (2017) 64–71.
- [32] O. E. Kalashev, V. A. Kuzmin, D. V. Semikoz and G. Sigl, *Ultrahigh-energy neutrino fluxes and their constraints*, *Physical Review D* **66** (2002) 063004.
- [33] H. Takami, K. Murase, S. Nagataki and K. Sato, *Cosmogenic neutrinos as a probe of the transition from galactic to extragalactic cosmic rays*, *Astroparticle Physics* **31** (2009) 201–211.
- [34] M. Ahlers and F. Halzen, *Minimal cosmogenic neutrinos*, *Physical Review D* **86** (2012) 083010.

- [35] K. Kotera, D. Allard and A. V. Olinto, *Cosmogenic neutrinos: parameter space and detectability from  $p\bar{e}v$  to  $z\nu$* , *Journal of Cosmology and Astroparticle Physics* **2010** (2010) 013.
- [36] J. Alvarez-Muniz, W. R. Carvalho and E. Zas, *Monte carlo simulations of radio pulses in atmospheric showers using zhaires*, *Astroparticle Physics* **35** (2012) 325–341.

## A Obtaining and using icemc

icemc can be obtained from the GitHub repository <https://github.com/anitaNeutrino/icemc>. The only mandatory requirement for the compilation of icemc is a ROOT [11] installation. The compilation can be executed via the Makefile or using the CMake structure.

To run icemc one needs to define two environment variables and add them to the global path:

- ICEMC\_SRC\_DIR should point to the directory where the source code is saved;
- ICEMC\_BUILD\_DIR should point to the directory where the executable programs are.

To run icemc one can simply do:

```
./icemc -i {inputFile} -o {outputDirectory} -r {runNumber}
-n {numberOfNeutrinos} -t {triggerThreshold} -e {energyExponent}
```

All of the parameters are optional and if they are not specified inputs from `inputs.conf` are used. The two standard input files for the ANITA-III and ANITA-IV flights come with the package.

The output directory contains a series of root files with information about all the neutrinos simulated, as well as a text file containing the neutrino survival efficiency at different stages of icemc, and the volumetric acceptance.

Other programs test a portion of the full icemc tool:

- `testThermalNoise` simulates only the thermal noise at the payload for a specific ANITA flight.
- `testInputAfterAntenna` simulates the injection of an RF impulse after the antenna feed; this program is used to produce trigger efficiency scans similar to the ones taken before each ANITA flight.
- `testWAIS` simulates the WAIS pulser as described in Subsection 7.2.2.

To produce ANITA-like output files and use more advanced features of icemc, the installation of `libRootFFTWrapper` (<https://github.com/nichol77/libRootFftwWrapper/>) and the ANITA `eventReaderRoot` (<https://github.com/anitaNeutrino/eventReaderRoot>) is necessary.